

## Architected lightweight, sound-absorbing, and mechanically efficient microlattice metamaterials by digital light processing 3D printing

Zhendong Li, Xinwei Li, Jun Wei Chua, Chong Heng Lim, Xiang Yu, Zhonggang Wang & Wei Zhai

To cite this article: Zhendong Li, Xinwei Li, Jun Wei Chua, Chong Heng Lim, Xiang Yu, Zhonggang Wang & Wei Zhai (2023) Architected lightweight, sound-absorbing, and mechanically efficient microlattice metamaterials by digital light processing 3D printing, *Virtual and Physical Prototyping*, 18:1, e2166851, DOI: [10.1080/17452759.2023.2166851](https://doi.org/10.1080/17452759.2023.2166851)

To link to this article: <https://doi.org/10.1080/17452759.2023.2166851>



© 2023 The Author(s). Published by Informa UK Limited, trading as Taylor & Francis Group



[View supplementary material](#)



Published online: 23 Jan 2023.



[Submit your article to this journal](#)



Article views: 3564



[View related articles](#)



[View Crossmark data](#)



Citing articles: 19 [View citing articles](#)

# Architected lightweight, sound-absorbing, and mechanically efficient microlattice metamaterials by digital light processing 3D printing

Zhendong Li<sup>a,b</sup>, Xinwei Li<sup>b</sup>, Jun Wei Chua<sup>b</sup>, Chong Heng Lim<sup>b</sup>, Xiang Yu<sup>c</sup>, Zhonggang Wang<sup>id</sup><sup>a</sup> and Wei Zhai<sup>b</sup>

<sup>a</sup>School of Traffic & Transportation Engineering, Central South University, Changsha, People's Republic of China; <sup>b</sup>Department of Mechanical Engineering, National University of Singapore, Singapore, Singapore; <sup>c</sup>Department of Mechanical Engineering, The Hong Kong Polytechnic University, Hong Kong SAR, People's Republic of China

## ABSTRACT

It is of significance, but still remains a key challenge, to attain excellent sound-absorbing and mechanical properties in a material simultaneously. To overcome this challenge, herein, novel multifunctional microlattice metamaterials based on a hollow truss-plate hybrid design are proposed and then realised by digital light processing 3D printing. Quasi-perfect sound absorption ( $\alpha > 0.999$ ) and broadband half-absorption have been measured. The sound-absorbing capacity is verified to be based on the designed cascaded Helmholtz-like resonators. Physical mechanisms behind the absorptive behaviours are fully revealed by numerical analyses. The present microlattices also display superior modulus and strength to the conventional cellular materials and modified microlattices, which is attributed to their near-membrane stress state of the plate architecture. The mechanically robust behaviour of the present microlattices in turn derives from the hollow struts. This work represents an effective approach for the design and engineering of multifunctional metamaterials through 3D printing.

## ARTICLE HISTORY

Received 2 November 2022  
Accepted 5 January 2023

## KEYWORDS

DLP; multifunctional metamaterial; microlattice; sound absorption; mechanical property


## 1. Introduction

Developing lightweight high-performance engineering materials has always been a significant task for various applications (Ha and Lu 2020; Zhang et al. 2015) such as military defense, aerospace, automotive, marine, etc. In recent years, the growth of additive manufacturing technologies has spurred interest in developing artificial metamaterials whose performances surpass those of the traditional materials. These metamaterials are featured by their artificial architectures realised by diverse design strategies such as bionic design and topology optimisation (Al-Ketan, Rowshan, and Abu Al-Rub 2018; Sha et al. 2021; Zhang et al. 2022, 2020), thereby exhibiting exotic and intriguing physical properties. A new class of materials, microlattices, are typical examples. Defined as periodic porous structures with elementary features such as strut, shell, plate, or combinations, microlattice metamaterials have small dimensional size but display unprecedented mechanical properties (Schaedler et al. 2011; Salari-Sharif, Valdevit, and Schaedler 2014; Clough et al. 2019). For instance, they possess excellent specific stiffness/strength as load-bearing materials

(Zhang et al. 2022), customisability in stiffness as self-adaptive materials (Fang et al. 2022), and high specific impact energy absorption ability as passive protective devices (Kai et al. 2022). Intrinsically, lattice structures present high design freedoms for customisable feature-pore morphology and interconnectivity, and thus they have been successfully developed for multifunctional application purposes. To name a few, recoverable energy absorption, tunable rigidity, and reconfigurable morphology by liquid metal lattice (Deng, Nguyen, and Zhang 2020); superior out-of-plane load-bearing capacities and broadband radar absorption characteristics (Zhang et al. 2021); band vibration suppression and sound absorption (An et al. 2021). These works all show efficient lattice designs with multifunctional considerations. Additionally, the developed generalised models for the purpose of topological optimisation or simulation have also contributed to the development of microlattice materials (Ciallella et al. 2022; Berezovski, Giorgio, and della Corte 2016; Abdoul-Anziz and Seppecher 2018).

Notwithstanding, facing the increasingly serious noises that exist in daily transportation, office, and

**CONTACT** Zhonggang Wang  wangzg@csu.edu.cn  School of Traffic & Transportation Engineering, Central South University, Changsha 410075, People's Republic of China; Wei Zhai  mpezwei@nus.edu.sg  Department of Mechanical Engineering, National University of Singapore, Singapore 117575, Singapore

 Supplemental data for this article can be accessed online at <https://doi.org/10.1080/17452759.2023.2166851>.

© 2023 The Author(s). Published by Informa UK Limited, trading as Taylor & Francis Group

This is an Open Access article distributed under the terms of the Creative Commons Attribution-NonCommercial License (<http://creativecommons.org/licenses/by-nc/4.0/>), which permits unrestricted non-commercial use, distribution, and reproduction in any medium, provided the original work is properly cited.

other constructions, typical microlattice metamaterials seemingly are incapable of mitigating the noise problem owing to their pale sound absorption performance (Sun, Jiang, and Wang 2020; Yang et al. 2020). Indeed, through the synthesis of advanced materials, the state-of-the-art foam materials have been proposed as sound absorbers, displaying superb sound absorption performance (Jia et al. 2020; Pang et al. 2022). Meanwhile, architected sound-absorbing metamaterials (Assouar et al. 2018; Shao et al. 2022; Ma et al. 2022) also represent radical advances in recent years. Some typical examples include Fabry-Pérot (FP) channel (Yang et al. 2017), embedded-neck assembly (Guo et al. 2020; Zhou et al. 2021), and micro-perforated panels (Wang et al. 2023; Li et al. 2021; Zeng et al. 2022). However, as compared to these sound absorbers, there are unique potential advantages of microlattice absorbers, that is, being structurally rigid, robust, customisable, and with the potential for multifunctionality (Deng, Nguyen, and Zhang 2020; Li et al. 2022; Li, Yu, and Zhai 2021; Li et al. 2021). It is a prevailing topic in the last two years to investigate the absorption capabilities of lattices materials. But the present reported microlattice absorbers attain the sound-absorbing capacity by structural porosity, as opposed to a specified acoustic mechanism-guided design, showing either a narrow bandwidth, low absorption coefficients, or both. For example, the introduced micro-pores for removing remained powders of metal plate-lattices can opportunely offer acoustic impedance, thereby presenting the flawed absorptive behaviours (Li et al. 2022; Li et al. 2021). While for sheet lattices, such as triply periodic minimal surface (TPMS), the sound absorption coefficient is undesired owing to the high interconnectivity of air phases (Yang et al. 2020).

It is thus of great significance to propose a reasonable architectural design for microlattice to attain superior

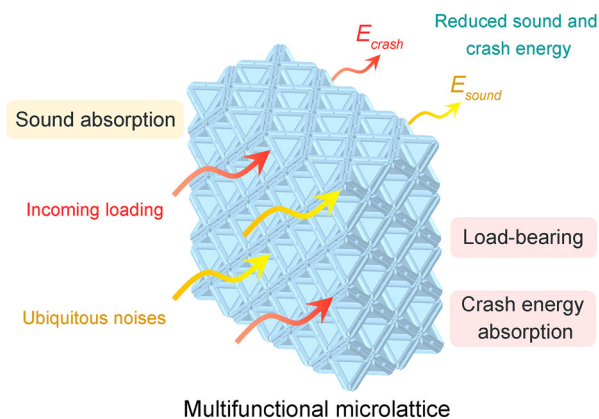


**Figure 1.** Schematic of the noise and crash energy hazards and a possible multifunctional microlattice to mitigate these problems simultaneously.

sound absorption and mechanical properties (schematically illustrated in Figure 1), for which the dual functionalities mutually complement in the intended application scenarios, such as airplane, automobile, military equipment, etc. Specifically, to achieve excellent sound absorption in a microlattice, one direction we can venture into is the inclusion of Helmholtz resonance mechanism (Assouar et al. 2018; Gao et al. 2022). With this in mind, adding plate architectures and perforations to a truss lattice could be an efficient approach to constitute Helmholtz resonators. As such, in consideration of lightweight property and mechanical robustness, we turn to investigations on the truss-plate hybrid microlattices whilst adopting the prevailing hollow octet-truss (HOT) lattice design motif as our basis for the present study.

Herein, we propose the lightweight multifunctional microlattices (LMMs) with superior sound-absorbing and mechanical properties. These LMMs are fabricated by digital light processing (DLP) 3D printing. Experimentally demonstrated, the microlattices realise the quasi-perfect sound absorption ( $\alpha > 0.999$ ) with a wide half-absorption (around 3.9 kHz). Besides, they can sustain the weight more than 30,000 times its own, display damage-tolerant behaviour, and offer superior modulus and strength to the conventional cellular materials and modified microlattices. The mechanisms underlying the sound-absorptive and mechanical responses are fully revealed.

## 2. Architectural design

Hollow design of lattice struts substantially improves the mechanical robustness of materials as compared to solid lattice materials (Salari-Sharif, Valdevit, and Schaedler 2014; Surjadi et al. 2021), which avoids the catastrophic failure when subjected to compression. This is manifested in our preliminary experiments for hollow octet-truss (HOT) and solid octet-truss (SOT) lattices (Figure S1, Supplementary Material). Nevertheless, the mechanical performance of HOT is still limited by the stress instability and low stress plateau. Moreover, the sound absorption tests show that HOT and SOT both exhibit poor sound absorption coefficient  $\alpha$  ranging from 1000 to 6300 Hz without obvious difference (Figure S2, Supplementary Material). As such, although HOT has been widely investigated owing to its outstanding damage tolerance, substantial improvements on its acoustic absorption and mechanical properties are highly desired. In this study, HOT is employed as the design motif in our lattice design, and the specific design guideline is illustrated below.

Before elaborating the proposed design strategy, the general requirements for achieving enhanced sound

absorption and mechanical performance are discussed. With regards to acoustic absorption, the HOT exhibits poor absorption because of the highly-interconnected air phase, as shown in Figure 2. This adversely affects sound absorption as no efficient damping mechanism is presented (Yang et al. 2020). To address this issue, its air phase needs to be reconfigured, such that an effective resonant system can be established to enhance the resonance-induced loss. Previously reported sound absorber metamaterials are mainly designed based on the Helmholtz resonator (Ma et al. 2022; Jiménez et al. 2016) – a typical structure composed of micro perforations and empty cavities. However, challenges still exist on how to introduce the HR mechanism to lattice structures at the microstructural level. As for the mechanical reinforcement, as analysed before, higher strength and plateau stability are desired for HOT. Berger et al. (Berger, Wadley, and McMeeking 2017) suggested that the plate-based lattice develop membrane stresses that efficiently utilise material volume independently of the macroscopic loading direction. Hence, it is intuitive to add plates to this truss lattice for enhanced mechanical performance.

As inferred from preceding analyses, a hybrid truss-plate architectural design strategy is proposed for simultaneous sound-absorbing and mechanical improvement, as plotted in Figure 2. Specifically, in Step 1, thin plates between adjacent struts are added as acoustic hard boundaries to separate the air phase. Given the special geometry, three plates of [111] family of planes are embedded to a 1/8-unit cell, while the plane connected to the central cavity maintains unchanged. Then, in Step 2, for a 1/8-unit, micro-perforations are constructed on the geometric centre and four corners in each

direction, i.e. [100], [010], and [111]. As such, the whole connected air phase is separated by narrow air channels. Eventually, mirroring the 1/8-unit, a complete LMM unit cell equipped with micro-perforations with associated cavity is obtained.  $t_a$ ,  $d_p$ , and  $l_0$  denote the thickness of plate, perforation diameter of perforations, and unit cell length, respectively. The outer and inner diameter of hollow struts are designated as  $d_1$  and  $d_2$ .

### 3. Materials and methods

#### 3.1. Fabrication by DLP

Additive manufacturing (AM) process enables the fabrication of complex structures with fine-features and internal geometries at the microscale to be possible. Some typical AM technologies, such two-photon lithography direct laser writing, self-propagating photopolymer waveguides, and direct ink writing, show compelling potentials in achieving maximised performance of modern products. Herein, all the microlattice specimens were fabricated by DLP technology (Asiga Max X27 DLP, Australia). The material in use was a 405 nm wavelength acrylate-based UV photosensitive resin composed of non-toxic acrylic polyester, from Nova3D, China. Filling up the resin tank, the build platform was vertically submerged into the tank. The UV laser emitted from an optical digital device traced the designed pattern of each layer, with 2D pattern formed on the platform. Hence, the microlattice pattern was attained by repeating this process layer by layer. After printing, the raw samples were thoroughly washed using isopropyl alcohol (IPA) for around 20 min to remove the excess resin, and then dried by a high-power blowing machine. After fully drying, the samples

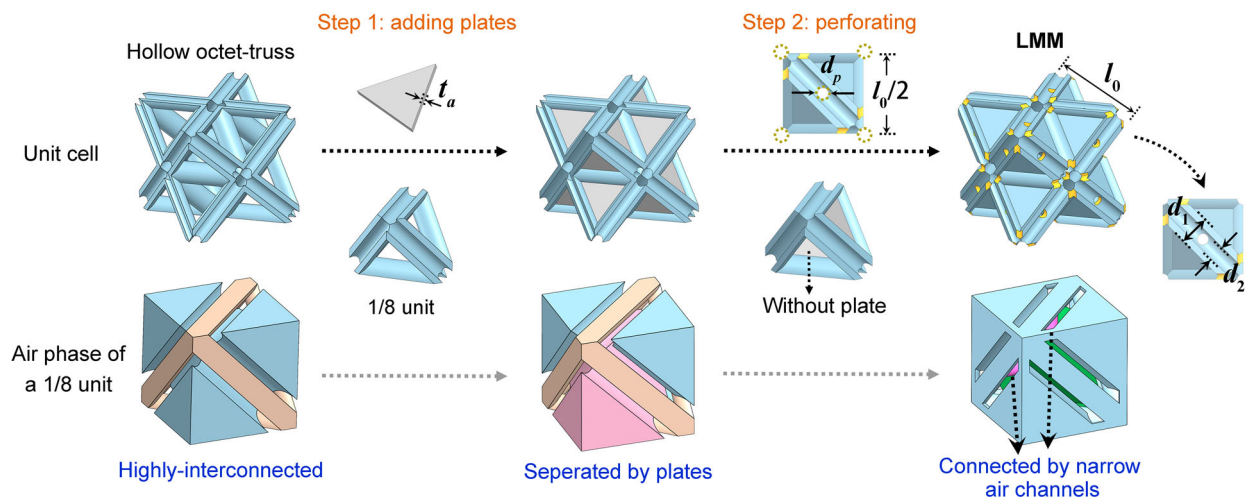


**Figure 2.** Architectural design for the purpose of realising superb sound-absorbing and mechanical performance simultaneously. Two design steps are illustrated: adding plates and perforating. The air phase of a 1/8-unit for each lattice configuration is compared. The highly-interconnected phase of HOT is transformed into a single phase connected by narrow air channels.

**Table 1.** The designed geometric parameters of LMMs (Unit: mm).

|       | $d_1$ | $d_2$ | $l_0$ | $t_a$ | $d_p$ |
|-------|-------|-------|-------|-------|-------|
| LMM-A | 1.3   | 0.3   | 7.0   | 0.3   | 0.5   |
| LMM-B | 1.3   | 0.5   | 7.0   | 0.3   | 0.5   |
| LMM-C | 1.3   | 0.7   | 7.0   | 0.3   | 0.5   |
| LMM-D | 1.3   | 0.9   | 7.0   | 0.3   | 0.5   |

were then post-cured in an ultraviolet chamber for 0.5 h, Asiga Flash. Main DLP printing parameters include a light intensity of  $5 \text{ mW}\cdot\text{cm}^{-2}$ , layer thickness of  $100 \mu\text{m}$ , and an exposure time of 1.5 s for each layer.

### 3.2. Geometry and characterisation

Specific geometric parameters of lattice specimens are given in Table 1. Herein, LMMs are classified into four groups by the hollow level of struts, i.e. varying inner tube diameter  $d_2$ . The suffix A, B, C, and D represent  $d_2 = 0.3, 0.5, 0.7,$  and  $0.9 \text{ mm}$ , respectively. All these microlattices consist of  $3 \times 3 \times 3$  cells, and each type is fabricated in triplicate (Figure S3, Supplementary Material). The measured densities of these specimens are shown in Table 2. Figure 3(a) shows the microstructural morphology of microlattices viewing from [001] plane by KEYENCE VHX-6000 digital microscope. There are no obvious fracture, burr, and fault-segmentation as observed. Figure 3 (b) shows the representative microstructural features of hollow struts and micro-pores. A small portion of the hollow struts of LMM-A is blocked, while other three specimens all show good printing precision. As the pore size is an important parameter for sound absorption, the actual pore size of as-printed specimens is measured by the microscope software. A large area covering 17 pores is selected for the measurement as shown in Figure 3(c). The measured data are shown in the column map (Figure 3(d)). It is found that all the pores possess slightly smaller diameter than the designed value of  $500 \mu\text{m}$ . This is attributed to the printing discrepancy for such a microscopic feature especially for the substrate layer. The averaged value of the measured diameters is  $425 \mu\text{m}$ , which will be used in the following analytical calculations.

### 3.3. Sound absorption tests

A two-microphone impedance tube (BSWA MPA416) setup in accordance to ISO 10534-2 standard was

**Table 2.** The measured densities of the as-printed lattices.

|   | LMM-A            | LMM-B            | LMM-C            | LMM-D            |
|---|------------------|------------------|------------------|------------------|
| Mass density ( $\text{g}/\text{cm}^3$ ) | $0.56 \pm 0.009$ | $0.52 \pm 0.004$ | $0.46 \pm 0.005$ | $0.37 \pm 0.008$ |
| Relative density (%)                    | $47 \pm 0.7$     | $44 \pm 0.4$     | $38 \pm 0.4$     | $31 \pm 0.6$     |

utilised for sound absorption coefficient measurements (Figure S4, Supplementary Material). The impedance tube has a diameter of 30 mm, providing valid testing frequency range from 0.8 to 6.3 kHz. To fit the lattice samples into the tube, they were extruded cut in CAD with a cylinder pattern with diameter of 30 mm. Specimens were rigidly backed in the sample holder and loaded at the end of the impedance tube. The tests for each sample were repeated multiple times and each reported absorption coefficient curve was averaged result from at least three measurements.

### 3.4. Compression tests

Compression tests for microlattice specimens were performed using Shimadzu AG25-TB universal testing machine at a strain rate of  $0.002 \text{ s}^{-1}$ . The parallel pair of faces in line with the DLP printing direction was orientated for compression. The microlattices were placed in the centre of the platen, and compressed by the moving rigid plate along the longitudinal direction until the specimen is densified. A digital camera was used for the capture of deformation modes. All tested data were reported in terms of three sets of averaged results with the error by their standard deviation.

## 4. Results and discussions

### 4.1. Experimental sound absorption performance

The experimentally measured sound absorption coefficient  $\alpha$  of LMMs are presented in Figure 4(a). Apparently, as compared to the absorption performance of SOT and HOT with  $\alpha$  around 0.6 (Figure S1, Supplementary Material), all LMMs exhibit higher peaks and wider absorption bandwidth. Two resonant peaks are observed, and the peak value of the first resonant frequency is higher than that of the second one. The highest  $\alpha$  is obtained by LMM-B. When frequency is 1750Hz,  $\alpha$  of LMM-B exceeds 0.999, reaching a quasi-perfect absorption (Romero-García et al. 2016; Duan et al. 2020). By fitting the measured data, Figure 4(b) plots the influence of hollow level of struts on sound-absorption performance. It is pronounced that the increasing  $d_2$  (inner diameter of struts) deflect both the first and the second absorptive peaks to higher frequencies, and interestingly, the peak value slightly goes down for the first peak while ascends for the second one. The sound absorption improvement brought from the present design are then demonstrated by the measured average  $\alpha$  over all the frequency range and the half-absorption bandwidth ( $B_{\alpha=0.5}$ ). Figure 5(a) compares the average  $\alpha$  of LMMs with that of SOT and HOT. For

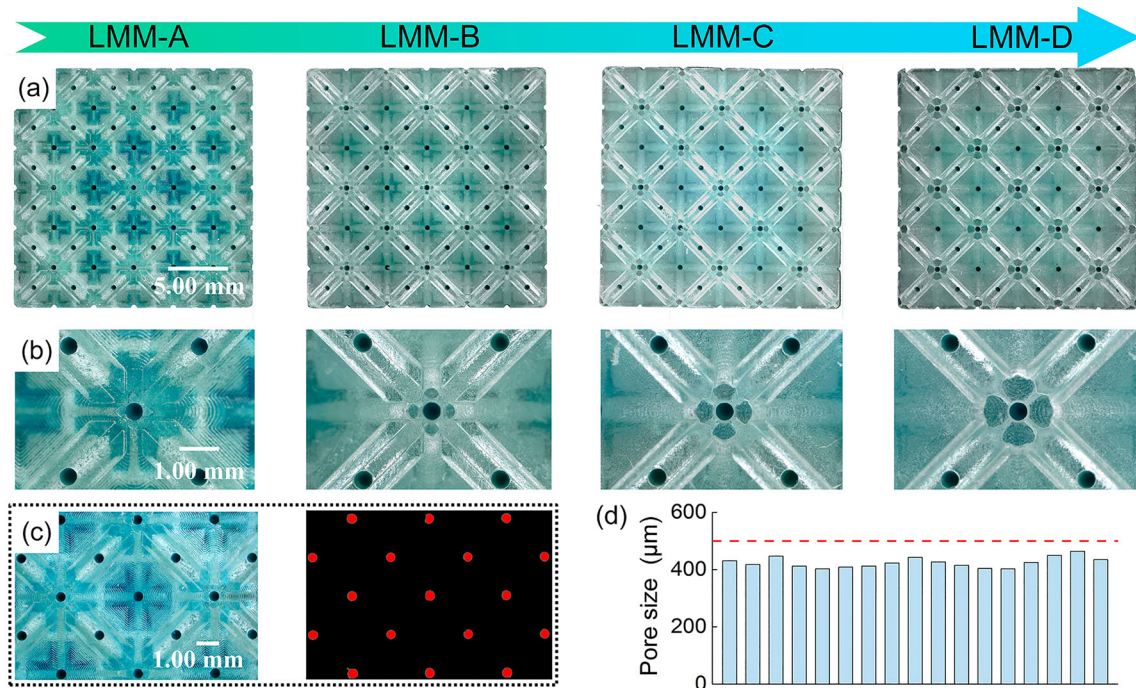


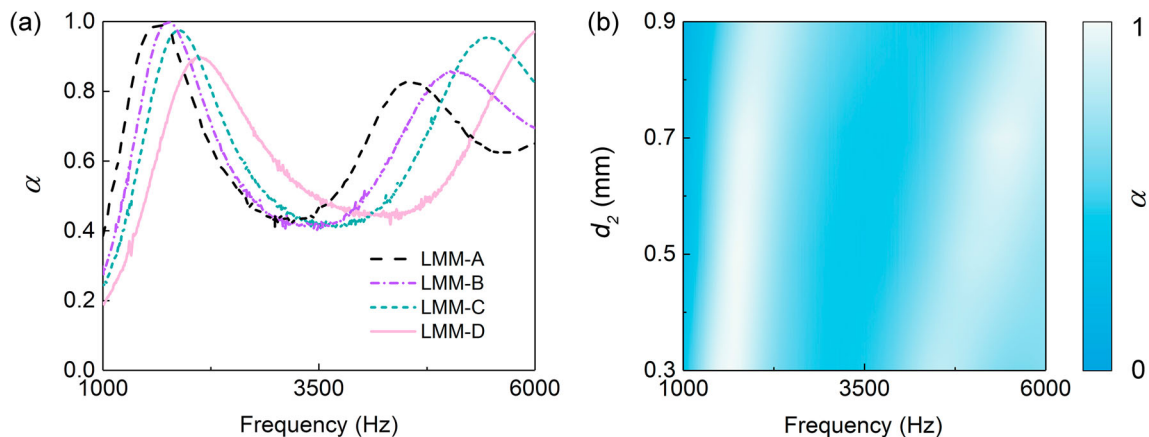
**Figure 3.** DLP-printed specimens and microscopic features. (a) Microstructural morphology of lattices viewing from [001] plane. (b) Representative microstructural features of hollow struts and micro-pores. (c) Representative area for actual pore size measurement. (d) Corresponding measured perforation diameters of as-printed lattices.

LMMs, the average  $\alpha$  stabilises from 0.63 to 0.66, and that of LMM-B is around 2.2 and 2.0 times over that of SOT and HOT, respectively. Also, a substantial improvement is observed in terms of the  $B_{\alpha=0.5}$ , as shown in Figure 5(b). Ranging from 1000 to 6000 Hz,  $B_{\alpha=0.5}$  of our LMMs occupies 62%–77%, while this proportion of SOT and HOT is only 15% and 11%, respectively. Generally, LMMs possess the close performance in terms of average  $\alpha$  and  $B_{\alpha=0.5}$  while exhibits a slight frequency shift in absorption spectra, and more importantly, they all show a substantial absorption improvement compared with that of SOT and HOT. The mechanisms

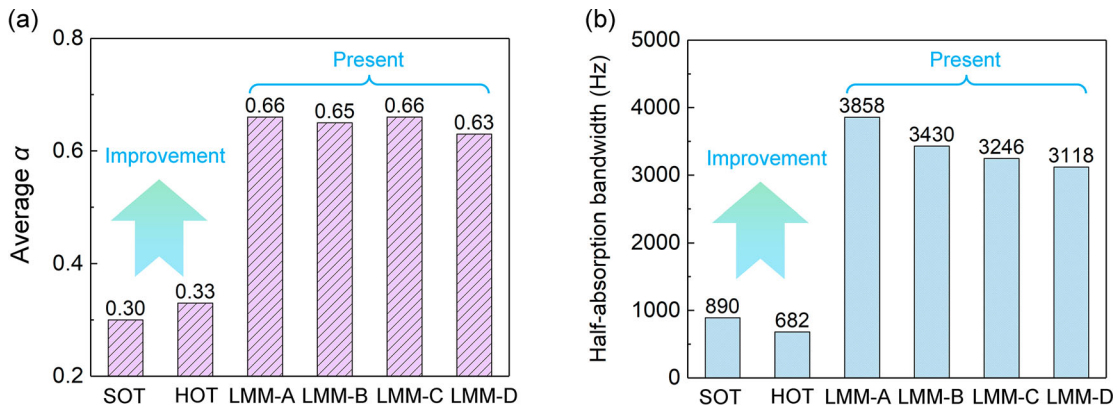
associated with these absorptive behaviours are discussed in the next section.

#### 4.2. Sound absorption mechanism

The sound wave attenuation capability of microlattice materials is based on the resonance effect (Li, Yu, and Zhai 2022). Herein, enabled by the designed Helmholtz resonant units for LMMs, effective resonance effect is obtained. To elucidate the resonant responses, a finite element model (FEM) of microlattice is constructed in COMSOL. The FE model is schematically plotted in



**Figure 4.** Experimentally measured sound absorption performance of LMMs. (a) Sound absorption coefficient ( $\alpha$ ) of LMMs from 1000–6000 Hz. (b) The influence of  $d_2$  on  $\alpha$  from 1000–6000 Hz.



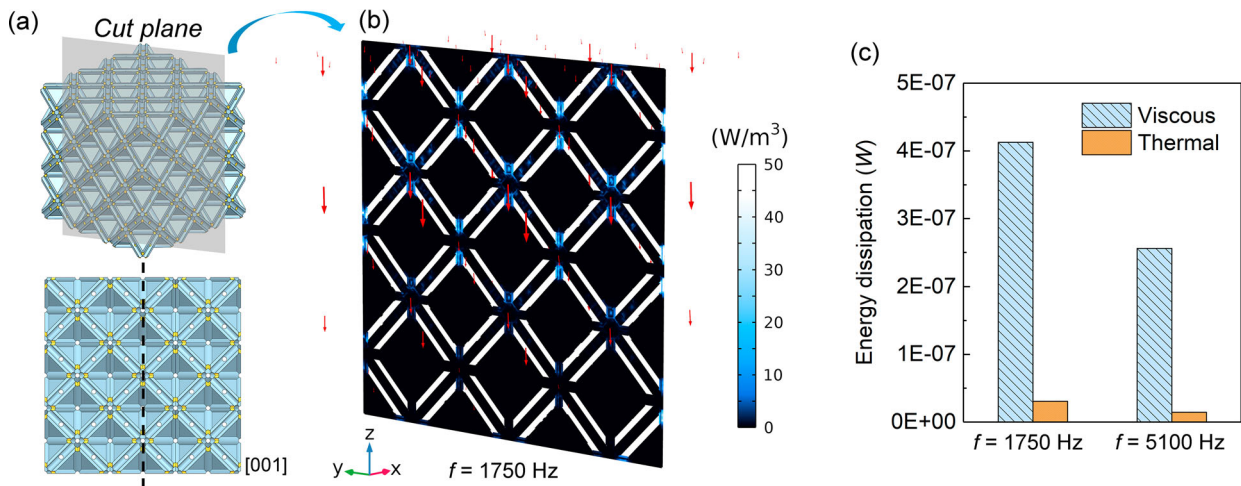
**Figure 5.** Enhancement of sound absorption. (a) Compared average sound absorption coefficient of SOT, HOT, and LMMs. (b) Compared half-absorption bandwidth of SOT, HOT, and LMMs.

Figure S5, with modelling details presented (Section S3, Supplementary Material). Herein, the simulation is employed for LMM-B as an example. Specifically, due to the perforations in microlattice being submillimeter scale, the thermo-loss and viscous loss should be responsible for the energy dissipation. Thus, in the simulation, the system is assumed as lossless and isentropic. The Navier-Stokes equation is linearised, and then the thermo-viscous effect is calculated by the continuity equation, momentum equation and energy conservation equation in thermo-viscous module, as respectively given by Equations (S1)–(S3), Supplementary Material.

A cut plane along the middle line of microlattice in [001] plane is selected to demonstrate the FE results (Figure 6(a)). Figure 6(b) shows the distribution map of total energy dissipation in the cut plane at the resonant frequency of 1750 Hz. It can be identified that most incident acoustic energy is dissipated in the vicinity of

perforations, while the dissipation by cavity is negligible. The red arrows, which represent the average velocity distribution of air, further verify that the air vibration mainly takes places in the perforations. The same phenomenon is also observed in the distribution map of air velocity and sound pressure in Figure S6, Supplementary Material. The velocity and pressure changes severely in the perforations rather than cavities. Like typical micro-perforated panels, (Wang et al. 2021; Duan et al. 2021; Tang et al. 2017) the energy dissipation (Figure 6(b)) and velocity (Figure S6(a), Supplementary Material) both show that the air particles vibrate more severely in the upper perforations, and then gradually decrease from the top to bottom.

Generally, owing the present architectural design, our microlattices dissipate sound energy based on Helmholtz resonance mechanism. The energy dissipation primarily occurs via the vibration-induced friction viscous loss



**Figure 6.** Demonstration of viscous and thermal dissipation with LMM-B as an example. (a) The selected cut plane along the middle line of microlattice. (b) The distribution map of total energy dissipation in the cut plane at the resonant frequency of 1750 Hz. The red arrows represent the average velocity distribution in microlattice. (c) Viscous and thermal dissipation values at the resonant frequencies of 1750 and 5100 Hz.

and thermal boundary layers. To be specific, Figure 6(c) compares their contributed values at resonant frequencies. As shown, viscous dissipation occupies around 93% and 95%, while the proportion of thermal dissipation is around 7% and 5%, at 1750 and 5100 Hz, respectively. In physics, the viscous boundary layers are formed because of the vibration and friction of air molecules when the incident wave passes through the micro-perforations, and thus the viscous dissipation  $W_v$  can be calculated as (Cops et al. 2019)  $W_v = 1/2(\eta v_t^2 / \phi_v)$ , where  $v_t$  denotes the tangential velocity with  $t$  of time evolution, and  $\phi_v$  denotes the viscous boundary layer. As such, viscous dissipation converts the sound energy into heat due to the severe air molecules' vibration, which also explains why the energy dissipation is more pronounced around the internal walls of perforations. Regarding thermal dissipation, physically speaking, it is induced by the breakdown of adiabatic propagation of sound waves. In other words, when airflow passes through the microlattice, the arising thermal boundary layers are responsible for the energy conversion and lost, and the dissipation is given by (Cops et al. 2019)  $W_t = 1/2(r - 1)p^2(w\chi/2\rho_0 C_p)^{0.5} / \rho_0 c_0^2$ , where  $\gamma$ ,  $p$ ,  $\chi$ , and  $C_p$  refers to the specific heat ratio, pressure outside of the boundary layer, thermal diffusivity, and specific heat capacity of air, respectively. To conclude, with sound waves flowing into the surface of microlattice, the air particles gather around the vicinity of micro-perforations, and then the airflow passes through the pores with dramatic air vibration, thereby impelling the viscous-thermal loss to damp sound waves into heat, with the sound intensity being diminished.

To uncover the underlying physics of sound absorption and elucidate the effect of hollow level of struts, acoustic impedance of LMMs under normal incident sound waves is analytically calculated based on electro-acoustic analogy method. Lateral pore connections are essentially neglected for airflow (Li, Yu, and Zhai 2021; Li et al. 2022). The present design enables a LMM unit cell to be working as a Helmholtz resonator. The air necks and cavity of a microlattice unit cell are marked in Figure 7(a), with specific parameters associated with impedance calculations annotated. The perforation pore size ( $d_p$ ) of as-printed specimens is illustrated in Section 3.2. Pore thickness ( $t_b$ ) is calculated by  $t_b = d_1/2$ . As the cavity is obtained based on octet-truss, the effective cavity length  $D_{eff}$  is calculated as  $D_{eff} = \sqrt[3]{V_{total} - V_{struts}}$ , where  $V_{total}$  and  $V_{struts}$  represent the volume of air phase inside the equivalent octet-plate lattice and the volume occupied by the microlattice struts, respectively. Surface porosity  $\sigma_l$  refers to the area of pores with respect to that of the non-porous area from [001] face. These parameters are

given in Table S1. As few air flows into the hollow struts, herein they are regarded as acoustic rigid boundaries. For our  $3 \times 3 \times 3$  microlattices, their resonant cells are equivalent to the series connection without parallel connection, and hence the periodical cells along [001] direction constitute a three-layer cascaded resonant system (Figure 7(a)).

The impedance of each layer is calculated based on acoustic-electric analogy method as follows. The acoustic impedance of micro-pores  $Z_{m,l}$  and cavities  $Z_{c,l}$  of  $l$ -th layer resonator are calculated. The surface impedance ( $Z_{s,l}$ ) is obtained as

$$Z_{s,l} = Z_{m,l} + Z_{c,l} \quad (1)$$

The impedance of micro-perforations  $Z_{m,i}$  is obtained as (Maa 1998; Li et al. 2021):

$$Z_{m,i} = \frac{32\eta t_p}{d_{p,i}^2 \sigma_l} \left( \sqrt{1 + \frac{\omega \rho_0 d_{p,i}^2}{128\eta}} + 2\lambda R_s \right) + j \frac{\omega \rho_0 t_p}{\sigma_l} \left( 1 + \left( 9 + \frac{\omega \rho_0 d_{p,i}^2}{8\eta} \right)^{-0.5} \right) + \frac{1}{\sigma_l} (0.85j\omega \rho_0 d_{p,i}) \quad (2)$$

where  $\omega$  denotes the angular frequency of incident sound wave and  $c_0$  denotes air velocity.  $\rho_0$  and  $\eta$  represent air density and dynamic viscosity, respectively.  $2\lambda R_s$  denotes the correction term for air flow friction with constants  $R_s = 1/2\sqrt{2\eta\rho_0\omega}$  (Ingard 1953) and  $\lambda$  is 2.0 for our case. The last term  $0.85j\omega\rho_0 d_{p,i}$  (Maa 1998; Tang et al. 2017) represents the end correction for mass reactance.

Then, the cavity impedance of  $l$ -th layer can be expressed in terms of

$$Z_{c,l} = \begin{cases} Z_0 \frac{Z_{l+1} \cos(kD_l) + jZ_0 \sin(kD_l)}{Z_0 \cos(kD_l) + jZ_{l+1} \sin(kD_l)}, & l = 1, 2, 3 \dots N-1 \\ -jZ_0 \cot(kD_l), & l = N \end{cases} \quad (3)$$

where  $k = \omega/c_0$  refers to the wavenumber and  $N$  refers to the total number of layers.

After calculating the impedance from layer 3 to layer 1, we then obtain  $\alpha$  under an incident sound wave as

$$\alpha = 1 - \left| \frac{Z_s/Z_0 - 1}{Z_s/Z_0 + 1} \right|^2 \quad (4)$$

where  $Z_s$  denotes the total surface impedance, and  $Z_0$  represents the characteristic impedance of air, calculated as  $Z_0 = \rho_0 c_0$ .

The calculated  $\alpha$  of LMMs by this analytical model agree very well with the measured data (Figure 7(b))



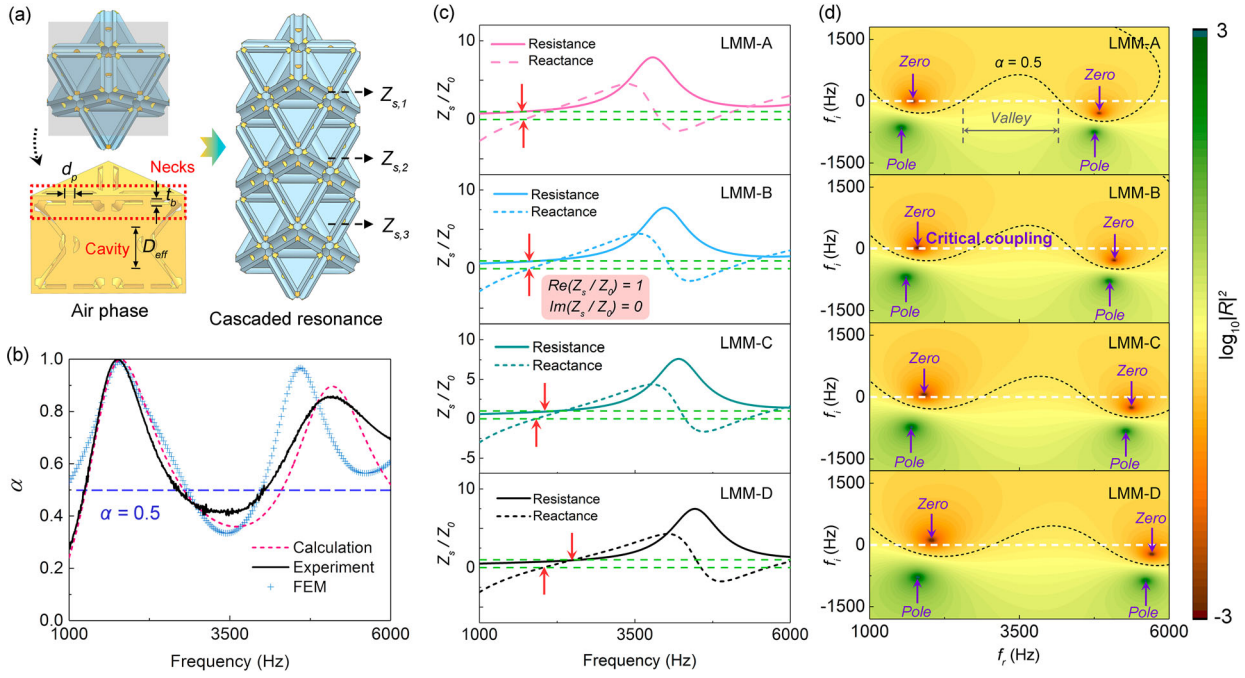


**Figure 7.** Physical mechanisms. (a) Air necks and cavity of a microlattice unit cell, geometric parameters for acoustic impedance calculations, and the three-layer cascaded resonant system. (b) Correlation between analytical calculation, experiment, and FEM in terms of sound absorption coefficient of LMM-B. (c) Relative impedance demonstrated by acoustic resistance and reactance, and (d) representation of the reflection coefficient in the complex frequency plane of LMMs with varying  $d_2$ .

and Figures S7–Figure S9, Supplementary Material). The curve of FEM also shows a close trend and peak values, with only a slight derivation on the second peak frequency. This derivation is mainly attributed to fabrication defects of samples as illustrated before. The dotted line refers to  $\alpha = 0.5$ , and the curves are above this line in most frequencies. As analysed before, the absorption mechanism is associated with the Helmholtz resonance effect. Herein, the impedance matching and damping behaviours are discussed to understand the underlying physics. Perfect absorption can be attained when the surface impedance equals to the impedance of air medium, that is, the real ( $\text{Re}(Z_s/Z_0)$ ) and imaginary parts ( $\text{Im}(Z_s/Z_0)$ ) simultaneously being equal to 1 and 0, respectively (Jiménez et al. 2016). Physically, the real and imaginary parts directly demonstrate the damping state and the peak frequencies, respectively. For the first peak, as shown in Figure 7(c), a well-matched impedance is observed for LMM-B, and this explains the quasi-perfect absorption performance in Figure 4(a). The second-best impedance matching state is offered by LMM-A, followed by LMM-C, and LMM-D, which exactly corresponds to the slight reduction of their peak values in Figure 4(a). The resistance of LMMs all keeps increases to a peak value, and then decreases to around 1.0 around the second resonant frequency. Besides, the discordant resistance peak keeps shifting to higher frequencies with the

rising  $d_2$ . Figure 7(d) physically illustrates the damping state by the distributions of  $\log_{10}|R|^2$  in the complex frequency plane (Romero-García et al. 2016; Jiménez et al. 2017), where  $R$  denotes the reflection coefficient. In the lossless case, the reflection coefficient contains a complex conjugate zero and a pole. Herein, for LMM-B, the zero locates around the real frequency axis at the first resonant frequency, generally reaching the critical coupling state. Thus, the energy loss and leakage in the system are greatly balanced. Corresponding to Figure 7(c), all the zeros of LMMs are below the real axis when coming to the second resonant frequency, and thus the system is over-damped, resulting in the relatively lower peaks (Figure 4(a)). The frequency domain where  $\alpha > 0.5$  is circled by the black dotted line and real frequency axis. It is observed that the absorption valley mainly locates around 3000–4000 Hz, which shift to higher frequencies when  $d_2$  increases.

### 4.3. Parametric analysis on sound absorption

#### 4.3.1. Effect of pore size

The diameter of perforations  $d_p$  in the above analyses was fixed as 0.5 mm. In fact, this value has a significant influence on sound absorption performance (Zhou et al. 2021; Duan et al. 2021; Maa 1998), hence its effect is discussed here by taking LMM-B as an

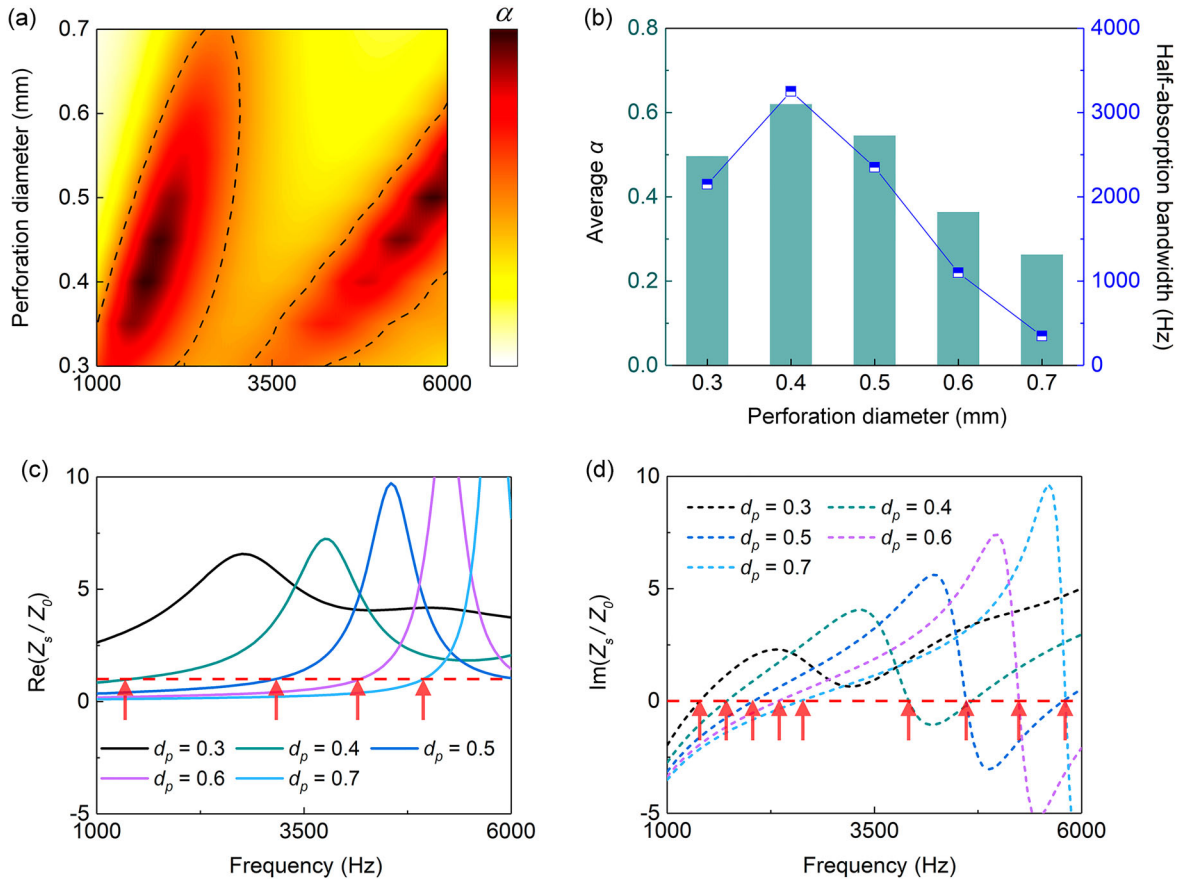


**Figure 8.** Analysis on the effect of pore size performed by analytical calculations. (a) The influence of perforation diameter (from 0.3–0.6 mm) on  $\alpha$  from 1000 to 6000 Hz. The black dotted curve represents  $\alpha = 0.5$ . (b) Compared average  $\alpha$  and half-absorption bandwidth, (c) resistance, and (d) reactance in the cases of five representative perforation diameters ( $d_p = 0.3, 0.4, 0.5, 0.6,$  and  $0.7$  mm).

example. The other geometric parameters are kept unchanged. Specifically, based on the derived model, the sound absorption coefficient  $\alpha$  is calculated with  $d_p$  changing from 0.3 to 0.7 mm, as depicted in Figure 8(a). As shown, when  $d_p$  ranges from 0.4 to 0.5 mm, high  $\alpha$  is obtained for both two peaks, indicating it is an ideal range for high absorption. However, with the rise of diameter, the absorption peak value decreases, e.g.  $d_p = 0.7$  mm. The compared average  $\alpha$  and half-absorption bandwidth of five representative perforation diameters in Figure 8(b) clearly demonstrates this regularity. The highest average  $\alpha$  and  $B_{\alpha=0.5}$  are obtained with  $d_p$  of 0.4 mm, while the rising diameter leads to a huge reduction on these two values. As illustrated in Section 4.2, the absorptive behaviours of the present microlattices are physically dependent on their impedance matching behaviour. Thus, the relative impedance is compared here for these varying diameters cases. Figure 8(c) shows that the increase of diameter results in severer fluctuation of resistance curves whose frequencies corresponding to  $Re(Z_s/Z_0) = 1$

soar to higher frequencies, and this is unmatched with the reactance trends (Figure 8(d)). Therefore, this extremely unmatched impedance behaviour reveals the reason for poorer absorption with the rising diameter.

#### 4.3.2. Heterogeneous arrangement of perforations

All the above findings in this study are based on a homogeneous arrangement of perforations. In other words, the perforation diameter  $d_p$  is identical in every layer of the microlattice. For the present  $3 \times 3 \times 3$  microlattice sound absorber, the heterogeneous arrangement of perforations is employed as shown in Figure 9. Along [001] direction, the diameter of each layer is designated as  $d_{p,1}$ ,  $d_{p,2}$ , and  $d_{p,3}$  from top to bottom, and hence they still produce the cascaded resonance. While for [100] and [010] directions, the resonators form the cascaded-parallel resonance instead. Note that the findings in section 4.3.1 indicate that the diameter of 0.4 mm is a proper value for a better absorption. As such, three representative cases, based on the diameter only changes in one specific layer

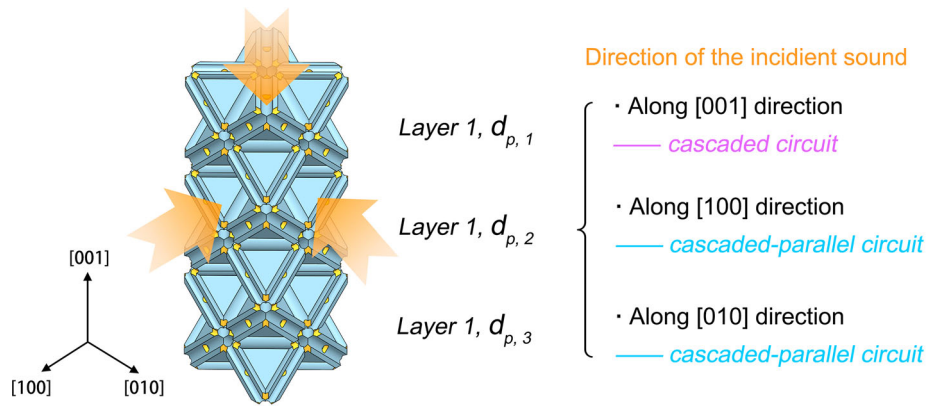


**Figure 9.** Heterogeneous arrangement of perforations and the resultant possible equivalent circuits (cascaded and cascaded-parallel) under varying incident sound direction.

with that of the other two layers equaling to 0.4 mm, are discussed here. Indeed, the possible arrangements are limitless, and machine learning based methods can be further developed to optimise the geometries in future work (Chen et al. 2022).

The case where sound wave flows along [001] direction is discussed here. With changing  $d_{p,1}$ ,  $d_{p,2}$ , and  $d_{p,3}$ , the absorption curves and relative impedance are demonstrated in Figure 10(a–c), respectively. Apparently, the diameter of 0.2 mm is an improper value for all these cases, especially for the first layer. As shown in Figure 10(a), when  $d_{p,1}$  equals to 0.2,  $\alpha$  is below 0.4 throughout the frequency range. The excessive surface

impedance under such a small diameter is responsible for this poor absorptive response. This finding also indicates that the first layer plays a more important role than the other two layers in impedance-matching performance. Besides, with the increase of diameter, the absorption curves are slightly deflected to higher frequencies, which results from the frequency shift of the corresponding relative impedance.

The present heterogeneous arrangement of perforations in Figure 9 empowers the microlattice to be capable of offering the combination of parallel and cascaded resonance when sound waves flow along [100] or [010] directions. Herein, a set of diameters optimised by

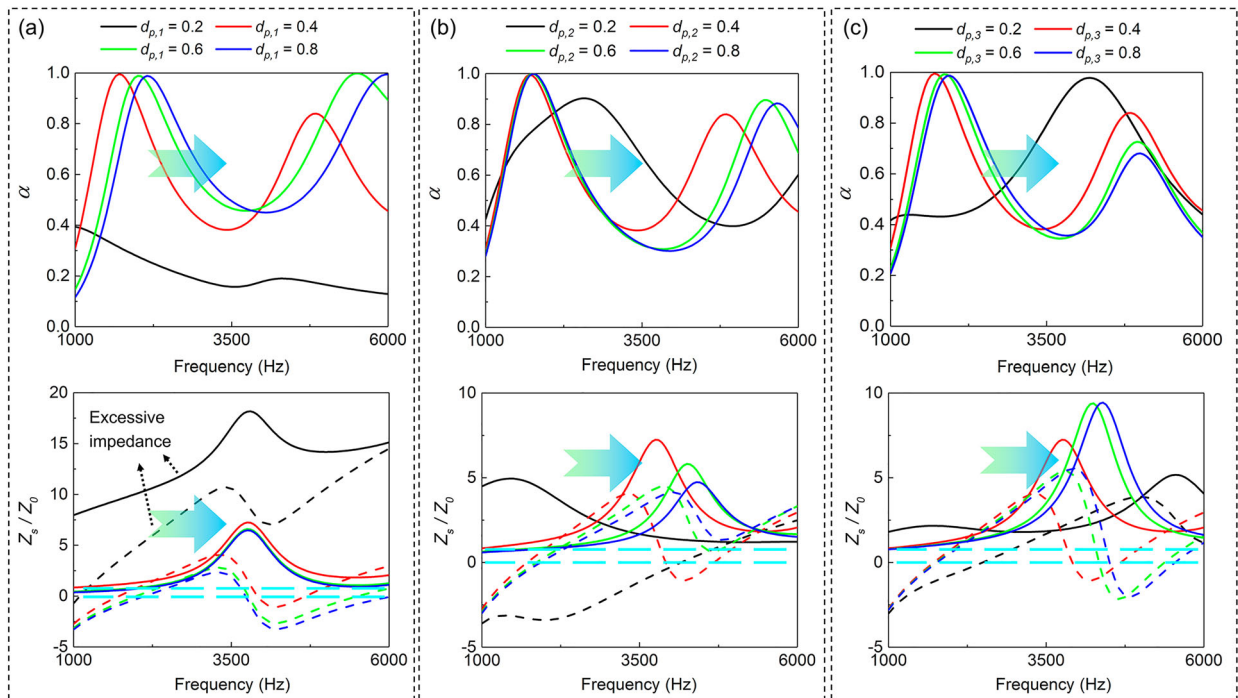


**Figure 10.** Analytically calculated absorption performance with sound waves flowing along [001] direction. Absorption curves and relative impedance with changing (a)  $d_{p,1}$ , (b)  $d_{p,2}$ , and (c)  $d_{p,3}$ .

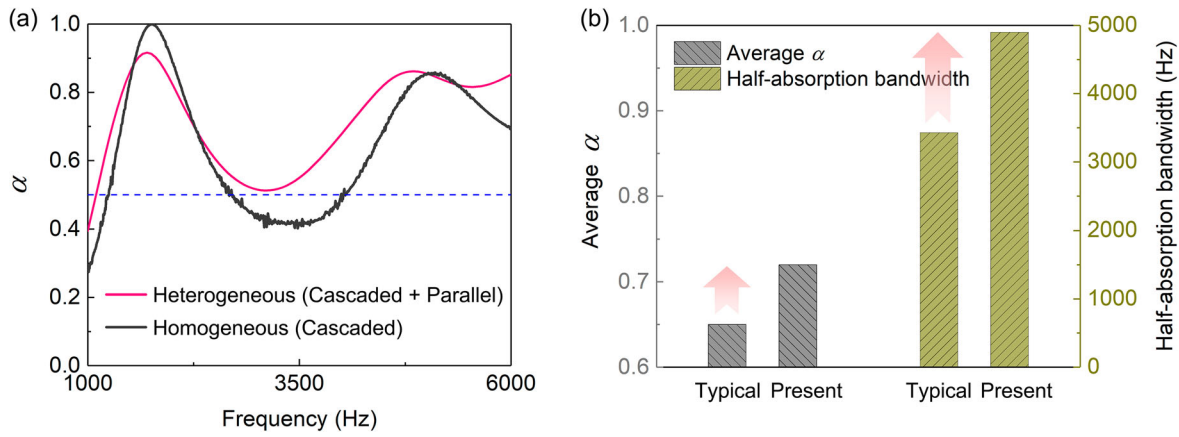


**Figure 11.** Absorption performance and enhancement of the present heterogeneous design with sound waves flowing along [100] or [010] directions predicted by analytical model. (a) Absorption curves in the case of heterogeneous arrangement with cascaded and parallel circuit, and the homogeneous arrangement with cascaded circuit. (b) Comparison of average  $\alpha$  and half-absorption bandwidth of the typical homogeneous design and the present heterogeneous design.

the analytical model is given as:  $d_{p,1} = 0.33$ ,  $d_{p,2} = 0.60$ , and  $d_{p,3} = 0.50$ , and the calculated absorption curve (in red) is shown in Figure 11(a), which shows higher  $\alpha$  in most frequencies as compared to the measured data of LMM-B with only cascaded resonance. Figure 11(b) intuitively plots the absorption improvement generated by the present heterogeneous design. With regards to average  $\alpha$ , it increases by 11% to a high value of 0.72. The half-absorption bandwidth improves by 43% to 4.9 kHz, indicating the absorption curve is above 0.5 almost in the whole frequency range.

Overall, the heterogeneous arrangement of perforations maximises the potentials of sound absorption performance of microlattice. The improvement in terms of sound absorption could be further enlarged by using machine learning method considering not only the pore size and heterogeneous arrangement, but also the unit cell geometry of microlattice, which deserves investigation in the future. Further, the heterogeneous arrangement of perforations would trigger

another interesting mechanical phenomenon, that is, the change of the deformation sequence of each layer under compression. The geometrical optimisation for both acoustic and mechanical improvement is a complex topic, which deserves exploration in the future.

#### 4.4. Compressive performance

As practical engineering materials, efficient mechanical responses such as high stiffness and strength, and damage-tolerant behaviour are highly-desired for microlattices. The compressive performance of LMMs is explored here. A set of experimentally measured stress–strain curves is shown in Figure 12(a). As shown, the hollow design enables LMMs to be damage-tolerant, that is, offering a long stress plateau, which avoids the premature and catastrophic failure of SOT, and at the meantime, the strength is substantially improved compared to that of HOT (Figure S1, Supplementary Material). Besides, with the rising  $d_2$ , the stress plateau

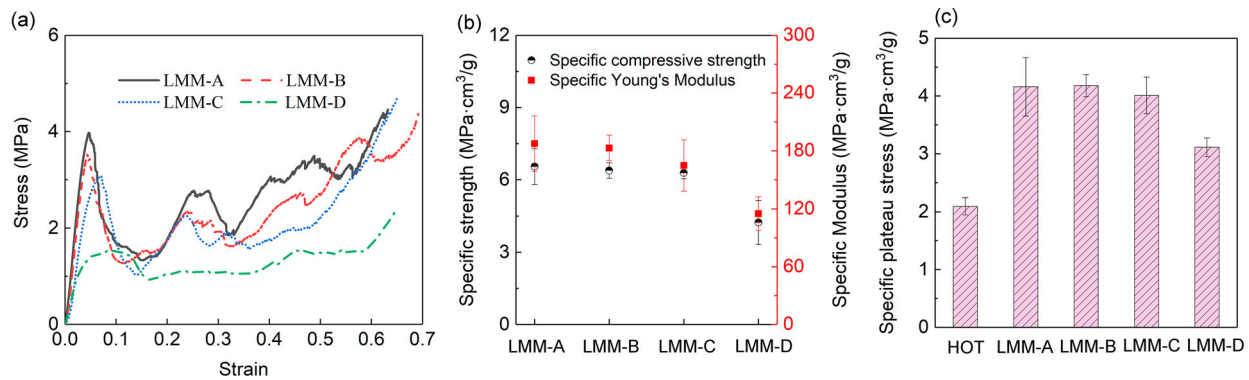


**Figure 12.** Experimentally measured compressive performance of LMMs. (a) A set of stress-strain curves. (b) Measured specific compressive strength and Young's modulus. (c) Comparison with HOT in terms of specific plateau stress.

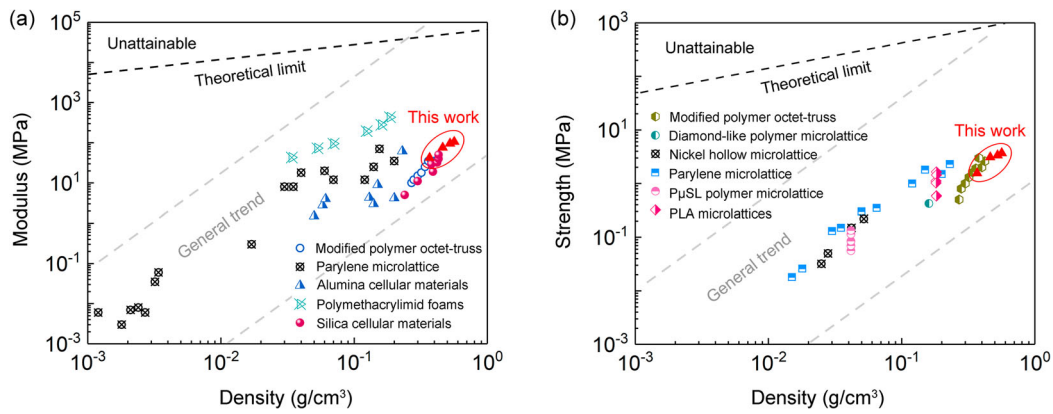


**Figure 13.** Modulus and strength scaling of cellular materials. (a) An Ashby chart exhibiting the modulus versus density for LMMs and other previously reported cellular materials. References used: modified octet-truss (Song et al. 2019), parylene microlattice (Maloney et al. 2013), alumina cellular materials (Kucheyev et al. 2006), polymethacrylimid foams (Maiti, Ashby, and Gibson 1984), and (Woignier et al. 1998). (b) An Ashby chart exhibiting the strength versus density for LMMs and other previously reported cellular materials. References used: modified octet-truss (Song et al. 2019), diamond-like polymer microlattice (Zhou et al. 2016), nickel hollow and parylene microlattice (Maloney et al. 2013), PμSL polymer microlattice (Dar et al. 2020), and PLA microlattices (Sun, Guo, and Shim 2021).

of LMMs gets a more flat plateau with less fluctuation, e.g. LMM-D. Based on the measured data, the averaged specific compressive strength and modulus of LMMs with standard deviations are given in Figure 12(b), showing a downward trend with the rise of  $d_2$ . But this also indicates that, with this hollow strut design, our LMMs are capable of offering on-demand strength and modulus by modulating the hollow level of struts. The specific plateau stress, calculated as the average specific stress with  $\varepsilon$  from 0.2 to 0.5 in the stable folding region, is calculated for HOT and LMMs in Figure 12(c). With varying hollow level, all LMMs have a specific strength over 3 MPa·cm<sup>3</sup>/g and higher than that of HOT. Taking LMM-B as an example, its specific plateau stress is double that of HOT. The dynamic loading tests with strain rate of 0.5 s<sup>-1</sup> were also performed for LMM-B. Compared with the quasi-static case, the yielding stress in such a dynamic loading is elevated substantially, which reveals the high sensitivity of strain rate of the base material (Figure S10, Supplementary Material).

The mechanical properties of LMMs are further evaluated by Ashby charts in Figure 13, where various lightweight cellular materials with different constituent, porosity, and geometry are compared. As shown in Figure 13(a), the present microlattices are relatively stiffer than the modified polymer octet-truss, parylene microlattice, alumina and silica cellular materials, even though the greatest performance is offered by the polymethacrylimid foams. Our LMMs all follow the general trend that the moduli are improved with the increase of density, thereby exhibiting this decent stiffness performance. Further, Figure 13(b) shows the compressive strength plotted against the density. As compared to

the previously reported polymer microlattices and nickel hollow microlattice, the present microlattices follow the general trend and exhibit higher strength. In brief, owing to the higher density of as-printed samples and the reinforcement brought from plate architectures, our LMMs possess higher modulus and strength than most of these cellular materials. The mechanisms associated with the efficient mechanical responses of LMMs are revealed in the next section.

#### 4.5. Deformation mechanisms

The deformation modes of LMMs with the compressive strain of 0, 0.15, 0.30, and 0.45 are shown in Figure 14 (a). As shown, LMM-A and LMM-B possess similar deformation features. Specifically, fractures firstly are observed around the pores with  $\varepsilon = 0.15$ . This phenomenon is predictable – an ultralow strain energy is needed for deformation for squeezing these pores. Hence, the introduced micro-perforations guide the preliminary and fractional fractures. Then, it comes to the local collapse of unit cells of a specific layer. When  $\varepsilon = 0.45$ , we found that there are some parts of lattices falling, marked by the yellow arrows. For LMM-C, a clear local shear band is observed, and this shear band keeps expanding with continuous loading, accompanying with the local collapse of unit cells. While for LMM-D, in such a high hollow level, interestingly, the plastic bending behaviour dominates the preliminary deformation. The reason is that, the hollow struts could be regarded as straw-like structure (Schaedler et al. 2011; Zheng et al. 2014) which substantially improves the damage tolerance. With successive loading, bearing, tearing, and folding of unit cells are observed. Then,

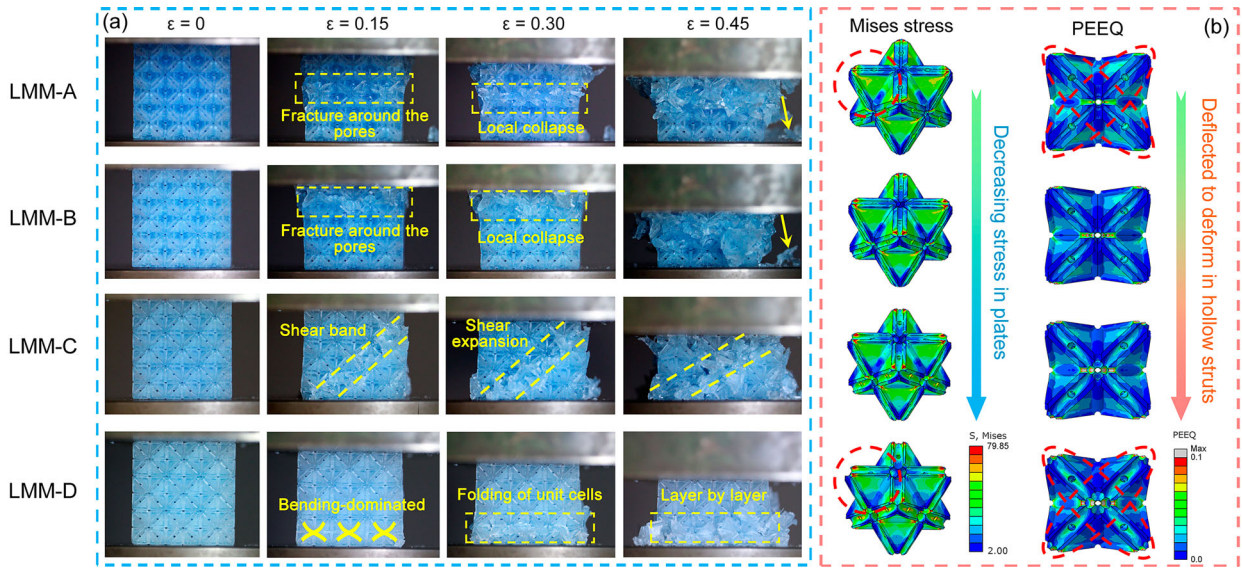


**Figure 14.** Deformation modes and mechanism. (a) Deformation modes of LMMs captured by digital camera with compressive strain of 0, 0.15, 0.30, and 0.45. (b) Finite element model analysis of a single unit cell of with compressive strain at 2%: Mises stress and equivalent plastic strain nephograms.

these microscopic deformation features eventually lead to the whole layer-by-layer collapse. Therefore, compared to the LMM-A, LMM-B, and LMM-C that show stretching-dominated deformation characteristics, the bending-dominated mode of LMM-D enables it to display a flat, stable, and long stress plateau and avoids the sharp drop of stress after yielding (Figure 12(a)).

Von Mises stress and equivalent plastic strain (PEEQ) distributions of LMMs are compared in Figure 14(b) via unit cell representations with compression strain of 2%. Note that FEM was employed mainly for the analysis and understanding of trends in stiffness and strength rather than the prediction of large-strain deformation (see details in Section S5, Supplementary Material). As shown, their different mechanical responses are attributed to the varying stress contributions owing to structural differences. It is noteworthy that, typical highly stretch-dominated truss structure shows concentrated stress on strut nodes and inclined struts (Li et al. 2021; Dong, Deshpande, and Wadley 2015), which leads to a low strain energy needed for deformation and hence catastrophic failure is easily to be observed. In contrast, the inclusion of plates of LMMs optimises the stress distribution and reaches a near-membrane stress state (Berger, Wadley, and McMeeking 2017). With successive loading, the high-stress spreads uniformly over the structure, and higher strain energy is needed for deformation. Therefore, this near-membrane stress state enables LMM to not only offer mechanical enhancement over HOT, but also to display higher modulus and strength than other truss-based microlattices. Besides, with the rising hollow level, it is found that the stress

of plates is decreasing. This phenomenon is more pronounced in the equivalent plastic strain (PEEQ) nephogram. From LMM-A to LMM-D, as shown by the red dotted line, the plastic strain around the pores located in the hollow struts increases substantially, while that of the plates, on the contrary, decreases. Therefore, such a large plastic strain in the neutral position of struts explains the unique bending feature and rupture of struts of LMM-D in Figure 14(a). Further, note that, the existence of microscopic pores guides the initial plastic deformation, which also improves the mechanical robustness of lattice materials to an extent.

## 5. Further discussion

### 5.1. Hollow level of struts

The present microlattice is composed of hollow truss and plate architectures. The above analysis has already indicated that the inclusion of plates is of great significance for enhancing the sound-absorbing and mechanical properties. Herein, the overall effect of the hollow level of struts is concluded and discussed. Based on the above measured data, the inner diameter  $d_2$  of hollow struts empowers the microlattice to be customizable in sound-absorbing and mechanical properties. Although  $d_2$  poses a slight effect on average  $\alpha$  and  $B_{\alpha=0.5}$  of LMMs, the rise of  $d_2$ , deems to deflect the trends of absorption spectra. Regarding to this phenomenon, as illustrated in Figure 2, the air phases of hollow struts and resonant cavity is connected, and thus the hollow struts herein influence the acoustic absorption

by surface porosities, which is illustrated in Section 4.2. From Figures 4 and 5, with varying  $d_2$ , the peak frequencies and values take changes although the average  $\alpha$  stabilises around 0.6 in these cases. In physics, the difference of peak values at the first resonant frequencies is ascribed to the different impedance matching states (Figure 7(c)). With rising  $d_2$ , the shift of discordant resistant peak as well as zeros in complex plane to higher frequencies reveal the physical essence for the shift of absorption curves. This fact is intuitively uncovered by the ‘mass-spring’ theory here. (Tang, Xin, and Lu 2019) To be specific, the ‘mass’ and the ‘stiffness of the spring’ can be calculated by  $m = \rho_0 t S$  and  $k = \rho_0 c_0^2 S^2 / V$  respectively. The resonance frequency is then given as

$$\omega_r = \sqrt{k/m} = c_0 \sqrt{S/Vt_p} \quad (5)$$

where  $S$  denotes the cross-sectional area of pores;  $t_p$ , and  $V$  represent the pore thickness and cavity volume. Hence, the rising  $d_2$  leads to the higher ‘stiffness of the spring’ in this system, and finally results in the larger  $\omega_r$ . For mechanical performance, the effect of hollow level is intuitively observed in the stress–strain curves in Figure 12(a). With rising  $d_2$ , the stress plateau is more flat without severe fluctuations, which owes to the bending-dominated deformation modes. The high hollow level enables the struts to be more like ‘straws’ (Zheng et al. 2014; Schaedler et al. 2011), and thus bending and folding of unit cells are dominant in the compression with less ruptures. In other words, the higher hollow level substantially enhances the damage tolerance of microlattice.

## 5.2. Advances and potentials

The scientific advances and potentials of the present microlattices are discussed here. With regards to sound absorption, our microlattices not only show substantial enhancement as compared to SOT and HOT, but also outperform the traditional sound-absorbing materials and advanced absorbers. Compared with conventional foam absorbers (Wang et al. 2022; Shao and Yan 2022; Hyuk Park et al. 2017; Cops et al. 2019), the present microlattices perform better in both absorption peak and half-absorption bandwidth. Specifically, our microlattices can achieve the quasi-perfect absorption ( $\alpha > 0.999$ ) and hit the half-absorption bandwidth up to 3.9 kHz as demonstrated experimentally. This exceptional absorption performance also outperforms that of the reported microlattice absorbers (Yang et al. 2020; Li et al. 2022; Li et al. 2021), in which the resonant cells are not designed for sound absorption purpose.

Besides, compared with all these aforementioned absorbers, our LMMs also offer distinct advantages in their favourable thickness —21 mm, which constitutes a notably high 30% reduction in thickness compared with the absorbers at 30 mm (Yang et al. 2019; Li, Yu, and Zhai 2021). Therefore, the proposed straightforward design concept in this study, that is, introducing the cascaded Helmholtz resonance mechanism to microlattice, represents an advance in designing advanced sound absorber. For its mechanical properties, the inclusion of plates optimises the stress contribution, and enables it to approach the approximate membrane stress body. As a result, our LMMs show higher specific strength than that of HOT (Figure 12(c)), and moreover, exhibit higher or comparable modulus and strength as compared to the reported polymer or metal-based microlattices (Figure 13(a) and (b)). Meanwhile, it is because the hollow design of struts is employed, LMMs display the damage-tolerant behaviour and avoid severe failure always found in solid truss lattices (Pham et al. 2019), or plate lattices (Andrew, Verma, and Kumar 2021; Andrew et al. 2021).

As practical engineering materials, the present microlattices are herein evaluated from the materials perspective. First of all, our microlattices possesses lightweight (0.37–0.56 g/cm<sup>3</sup>) property and multifunctionality. Note that the excellent sound absorption and mechanical properties could not be simultaneously realised by the aforementioned sound-absorbing material (e.g. foam and fibres) and advanced absorber metamaterials. Specifically, as load-bearing products, our LMMs can sustain the weight more than 30,000 times its own. From the pristine phase to post-yield phase, they can dissipate the crash energy by stable folding behaviour. As compared to the highly directional sandwich panels, the LMMs possess superior sound-absorbing and mechanical performance in in-plane directions, and the sound-absorbing performance could be further improved by heterogeneous arrangement of perforations (Figure 11). Additionally, it is noteworthy that the relative density has a great impact on the mechanical properties of microlattices, whilst the acoustic absorption depends on the microscopic geometries (e.g. diameter and thickness of pores) that have negligible influence on relative density. Thus, for practical products, the relative density can be determined based on the requirements of mechanical properties at the beginning, and then it comes to the microscopic geometry modulation for the desired sound absorption.

The present microlattices have great potentials in transportations, constructions, and other indoor settings for the purpose of both load-bearing and noises reduction. Additionally, it is worth noting that the

present architectural design is not limited to the applied polymer. By compromising the lightweight property, the proposed design can be extended for other engineering applications via the metal-based materials. For example, as high-strength load-bearing materials, or passive crash energy absorbers, the base material could be aluminium alloy, stainless steel, iron, nickel, etc. In this way, based on the measured data (Figure 13), it is speculated that the microlattice can also display ultra-strong mechanical properties.

## 6. Conclusion

In this work, lightweight multifunctional microlattices (LMMs) are proposed for achieving simultaneous excellent sound absorption and mechanical properties. These microlattices are fabricated by digital light processing 3D printing. The experimental results show that LMMs offer quasi-perfect absorption ( $\alpha > 0.999$ ) at the absorption peak, an average  $\alpha$  around 0.66, and wide half-absorption up to around 3.9 kHz. All LMMs exhibit substantial enhancement on sound absorption compared with the unmodified microlattices. Based on the numerical analyses, we validate that the sound-absorbing capacity is attributed to the viscous frictional flow and thermal boundary layers based on the designed cascaded resonant units. The unique absorptive behaviours and the influence of hollow level of struts are elucidated by the impedance-matching state and damping conditions. Also, compared with hollow octet-truss, the present microlattices display great improvement in specific strength. Superior modulus and strength of our LMMs to the conventional cellular materials and other modified microlattices are also observed in Ashby maps. These mechanical reinforcement and superiorities are then revealed by the approximate membrane stress state of the plate architecture, whilst the damage-tolerant behaviour is elucidated by the hollow level of struts. Overall, our LMMs are demonstrated to be lightweight, sound-absorbing, and mechanically efficient materials. This work may have implications for developing multifunctional materials by 3D printing.

## Disclosure statement

No potential conflict of interest was reported by the author(s).

## Funding

This work was financially supported by the National Natural Science Foundation of China [grant number 51875581]; NUS R&G Postdoc Fellowship Program [grant number A-0000065-25-00].

## Data availability

The data that support the findings of this study are available from the corresponding author upon reasonable request.

## ORCID

Zhonggang Wang  <http://orcid.org/0000-0003-1265-2762>

## Notes on contributors

**Zhendong Li** is a Ph.D. candidate in the School of Traffic & Transportation Engineering at Central South University, and a visiting Ph.D. student at ZhaiGroup@NUS, the Department of Mechanical Engineering at the National University of Singapore. His research interests include multifunctional materials, additive manufacturing, etc.

**Xinwei Li** is a research fellow at ZhaiGroup@NUS, the Department of Mechanical Engineering at the National University of Singapore. His research interests include additive manufacturing, lattice structures, and finite element modeling, with a focus on lightweight, energy absorption, and acoustics applications.

**Jun Wei Chua** is a Ph.D. candidate at ZhaiGroup@NUS, the Department of Mechanical Engineering, National University of Singapore. He studies additive manufacturing and acoustic materials.

**Chong Heng Lim** is a research fellow at ZhaiGroup@NUS, the Department of Mechanical Engineering, National University of Singapore. His research interests include additive manufacturing, lattice structures, etc.

**Xiang Yu** is an assistant professor at the Department of Mechanical Engineering, the Hong Kong Polytechnic University. His research interests include vibroacoustic modeling, sound and vibration control, acoustic metamaterials, and advanced functional materials.

**Zhonggang Wang** is a professor in Central South University. He leads a research group on impact dynamics, multi-physics coupling and control, novel composites, hierarchical materials, advanced functional materials, etc.

**Wei Zhai** is an assistant professor from the Department of Mechanical Engineering at the National University of Singapore. She leads the ZhaiGroup@NUS, developing nature-inspired advanced materials engineering via multi-scale and multi-material manufacturing technologies.

## References

- Abdoul-Anziz, Houssam, and Pierre Seppecher. 2018. "Strain Gradient and Generalized Continua Obtained by Homogenizing Frame Lattices." *Mathematics and Mechanics of Complex Systems* 6 (3): 213–250. doi:10.2140/memocs.2018.6.213.
- Al-Ketan, Oraib, Reza Rowshan, and Rashid K. Abu Al-Rub. 2018. "Topology-Mechanical Property Relationship of 3D Printed Strut, Skeletal, and Sheet Based Periodic Metallic Cellular



- Materials." *Additive Manufacturing* 19: 167–183. doi:10.1016/j.addma.2017.12.006.
- An, Xiyue, Changliang Lai, Weiping He, and Hualin Fan. 2021. "Three-Dimensional Chiral Meta-Plate Lattice Structures for Broad Band Vibration Suppression and Sound Absorption." *Composites Part B: Engineering* 224: 109232. doi:10.1016/j.compositesb.2021.109232.
- Andrew, J. Jefferson, Johannes Schneider, Jabir Ubaid, R. Velmurugan, N. K. Gupta, and S. Kumar. 2021. "Energy Absorption Characteristics of Additively Manufactured Plate-Lattices Under Low-Velocity Impact Loading." *International Journal of Impact Engineering* 149: 103768. doi:10.1016/j.ijimpeng.2020.103768.
- Andrew, J. Jefferson, Pawan Verma, and S. Kumar. 2021. "Impact Behavior of Nanoengineered, 3D Printed Plate-Lattices." *Materials and Design* 202: 109516. doi:10.1016/j.matdes.2021.109516.
- Assouar, Badreddine, Bin Liang, Ying Wu, Yong Li, Jian Chun Cheng, and Yun Jing. 2018. "Acoustic Metasurfaces." *Nature Reviews Materials* 3 (12): 460–472. doi:10.1038/s41578-018-0061-4.
- Berezovski, Arkadi, Ivan Giorgio, and Alessandro della Corte. 2016. "Interfaces in Micromorphic Materials: Wave Transmission and Reflection with Numerical Simulations." *Mathematics and Mechanics of Solids* 21 (1): 37–51. doi:10.1177/1081286515572244.
- Berger, J. B., H. N. G. Wadley, and R. M. McMeeking. 2017. "Mechanical Metamaterials at the Theoretical Limit of Isotropic Elastic Stiffness." *Nature* 543 (7646): 533–537. doi:10.1038/nature21075.
- Chen, An, Zi Xiang Xu, Bin Zheng, Jing Yang, Bin Liang, and Jian Chun Cheng. 2022. "Machine Learning-Assisted Low-Frequency and Broadband Sound Absorber with Coherently Coupled Weak Resonances." *Applied Physics Letters* 120: 3. doi:10.1063/5.0071036.
- Ciallella, Alessandro, Ivan Giorgio, Simon R. Eugster, Nicola L. Rizzi, and Francesco dell'Isola. 2022. "Generalized Beam Model for the Analysis of Wave Propagation with a Symmetric Pattern of Deformation in Planar Pantographic Sheets." *Wave Motion (North-Holland Publishing Company)* 113 (August): 102986. doi:10.1016/j.wavemoti.2022.102986.
- Clough, Eric C., Thomas A. Plaisted, Zak C. Eckel, Kenneth Cante, Jacob M. Hundley, and Tobias A. Schaedler. 2019. "Elastomeric Microlattice Impact Attenuators." *Matter* 1 (6): 1519–1531. doi:10.1016/j.matt.2019.10.004.
- Cops, Mark J., J. Gregory McDaniel, Elizabeth A. Magliula, and David J. Bamford. 2019. "Analysis of Thermal and Viscous Boundary Layers in Acoustic Absorption by Metallic Foam." *The Journal of the Acoustical Society of America* 146 (1): 649–655. doi:10.1121/1.5119224.
- Dar, Uzair Ahmed, Haris Hameed Mian, Muhammad Abid, Ameen Topa, Muhammad Zakir Sheikh, and Muhammad Bilal. 2020. "Experimental and Numerical Investigation of Compressive Behavior of Lattice Structures Manufactured Through Projection Micro Stereolithography." *Materials Today Communications* 25: 101563. doi:10.1016/j.mtcomm.2020.101563.
- Deng, Fanghang, Quang Kha Nguyen, and Pu Zhang. 2020. "Multifunctional Liquid Metal Lattice Materials Through Hybrid Design and Manufacturing." *Additive Manufacturing* 33: 101117. doi:10.1016/j.addma.2020.101117.
- Dong, Liang, Vikram Deshpande, and Haydn Wadley. 2015. "Mechanical Response of Ti-6Al-4V Octet-Truss Lattice Structures." *International Journal of Solids and Structures* 60: 107–124. doi:10.1016/j.ijsolstr.2015.02.020.
- Duan, Mingyu, Chenlei Yu, Fengxian Xin, and Tian Jian Lu. 2021. "Tunable Underwater Acoustic Metamaterials via Quasi-Helmholtz Resonance: From Low-Frequency to Ultra-Broadband." *Applied Physics Letters* 118 (7): 071904. doi:10.1063/5.0028135.
- Duan, Mingyu, Chenlei Yu, Zhimin Xu, Fengxian Xin, and Tian Jian Lu. 2020. "Acoustic Impedance Regulation of Helmholtz Resonators for Perfect Sound Absorption via Roughened Embedded Necks." *Applied Physics Letters* 117: 15. doi:10.1063/5.0024804.
- Fang, Xin, Jihong Wen, Li Cheng, Dianlong Yu, Hongjia Zhang, and Peter Gumbsch. 2022. "Programmable Gear-Based Mechanical Metamaterials." *Nature Materials* 21 (8): 869–876. doi:10.1038/s41563-022-01269-3.
- Gao, Nansha, Zhicheng Zhang, Jie Deng, Xinyu Guo, Baozhu Cheng, and Hong Hou. 2022. "Acoustic Metamaterials for Noise Reduction: A Review." *Advanced Materials Technologies* 7 (6): 2100698. doi:10.1002/admt.202100698.
- Guo, Jingwen, Xin Zhang, Yi Fang, and Ziyang Jiang. 2020. "A Compact Low-Frequency Sound-Absorbing Metasurface Constructed by Resonator with Embedded Spiral Neck." *Applied Physics Letters* 117: 22. doi:10.1063/5.0031891.
- Ha, Ngoc San, and Guoxing Lu. 2020. "A Review of Recent Research on Bio-Inspired Structures and Materials for Energy Absorption Applications." *Composites Part B: Engineering* 181: 107496. doi:10.1016/j.compositesb.2019.107496.
- Hyuk Park, Ju, Kyung Suh Minn, Hyeong Rae Lee, Sei Hyun Yang, Cheng bin Yu, Seong Yeol Pak, Chi Sung Oh, Young Seok Song, Yeon June Kang, and Jae Ryoung Youn. 2017. "Cell Openness Manipulation of Low Density Polyurethane Foam for Efficient Sound Absorption." *Journal of Sound and Vibration* 406: 224–236. doi:10.1016/j.jsv.2017.06.021.
- Ingard, Uno. 1953. "On the Theory and Design of Acoustic Resonators." *Journal of the Acoustical Society of America* 25 (6): 1037–1061. doi:10.1121/1.1907235.
- Jia, Chao, Lei Li, Ying Liu, Ben Fang, He Ding, Jianan Song, Yibo Liu, et al. 2020. "Highly Compressible and Anisotropic Lamellar Ceramic Sponges with Superior Thermal Insulation and Acoustic Absorption Performances." *Nature Communications* 11: 1. doi:10.1038/s41467-020-17533-6.
- Jiménez, N., W. Huang, V. Romero-García, V. Pagneux, and J. P. Groby. 2016. "Ultra-Thin Metamaterial for Perfect and Quasi-Omnidirectional Sound Absorption." *Applied Physics Letters* 109 (12): 121902. doi:10.1063/1.4962328.
- Jiménez, Noé, Vicent Romero-García, Vincent Pagneux, and Jean Philippe Groby. 2017. "Rainbow-Trapping Absorbers: Broadband, Perfect and Asymmetric Sound Absorption by Subwavelength Panels for Transmission Problems." *Scientific Reports* 7 (1), doi:10.1038/s41598-017-13706-4.
- Kai, Liu, Cao Xiaofei, Zhang Peng, Wu WenWang, and Li Ying. 2022. "Dynamic Mechanical Performances of Enhanced Anti-Tetra-Chiral Structure with Rolled Cross-Section Ligaments Under Impact Loading." *International Journal of Impact Engineering* 166: 104204. doi:10.1016/j.ijimpeng.2022.104204.
- Kucheyev, S. O., T. F. Baumann, C. A. Cox, Y. M. Wang, J. H. Satcher, A. v. Hamza, and J. E. Bradby. 2006.

- "Nanoengineering Mechanically Robust Aerogels via Control of Foam Morphology." *Applied Physics Letters* 89 (4): 041911. doi:10.1063/1.2236222.
- Li, Zhendong, Zhonggang Wang, Zichao Guo, Xinxin Wang, and Xifeng Liang. 2021. "Ultra-Broadband Sound Absorption of a Hierarchical Acoustic Metamaterial at High Temperatures." *Applied Physics Letters* 118 (16): 161903. doi:10.1063/5.0044656.
- Li, Xinwei, Xiang Yu, Jun Wei Chua, Heow Pueh Lee, Jun Ding, and Wei Zhai. 2021. "Microlattice Metamaterials with Simultaneous Superior Acoustic and Mechanical Energy Absorption." *Small* 17 (24): 2100336. doi:10.1002/smll.202100336.
- Li, Xinwei, Xiang Yu, and Wei Zhai. 2021. "Additively Manufactured Deformation-Recoverable and Broadband Sound-Absorbing Microlattice Inspired by the Concept of Traditional Perforated Panels." *Advanced Materials* 33 (44): 2104552. doi:10.1002/adma.202104552.
- Li, Xinwei, Xiang Yu, and Wei Zhai. 2022. "Less Is More: Hollow-Truss Microlattice Metamaterials with Dual Sound Dissipation Mechanisms and Enhanced Broadband Sound Absorption." *Small* 18 (44): 2204145. doi:10.1002/smll.202204145.
- Li, Zhendong, Wei Zhai, Xinwei Li, Xiang Yu, Zichao Guo, and Zhonggang Wang. 2022. "Additively Manufactured Dual-Functional Metamaterials with Customisable Mechanical and Sound-Absorbing Properties." *Virtual and Physical Prototyping* 17 (4): 864–880. doi:10.1080/17452759.2022.2085119.
- Ma, Fuyin, Chang Wang, Yang Du, Zicai Zhu, and Jiu Hui Wu. 2022. "Enhancing of Broadband Sound Absorption Through Soft Matter." *Materials Horizons* 9: 653–662. doi:10.1039/d1mh01685g.
- Maa, Dah-You. 1998. "Potential of Microperforated Panel Absorber." *The Journal of the Acoustical Society of America* 104 (5): 2861–2866. doi:10.1121/1.423870.
- Maiti, S. K., M. F. Ashby, and L. J. Gibson. 1984. "Fracture Toughness of Brittle Cellular Solids." *Scripta Metallurgica* 18 (3): 213–217. doi:10.1016/0036-9748(84)90510-6.
- Maloney, Kevin J., Christopher S. Roper, Alan J. Jacobsen, William B. Carter, Lorenzo Valdevit, and Tobias A. Schaedler. 2013. "Microlattices as Architected Thin Films: Analysis of Mechanical Properties and High Strain Elastic Recovery." *APL Materials* 1 (2): 022106. doi:10.1063/1.4818168.
- Pang, Kai, Xiaoting Liu, Jintao Pang, Akram Samy, Jin Xie, Yingjun Liu, Li Peng, Zhen Xu, and Chao Gao. 2022. "Highly Efficient Cellular Acoustic Absorber of Graphene Ultrathin Drums." *Advanced Materials* 34 (14): 2103740. doi:10.1002/adma.202103740.
- Pham, Minh Son, Chen Liu, Iain Todd, and Jedsada Lertthanasarn. 2019. "Damage-Tolerant Architected Materials Inspired by Crystal Microstructure." *Nature* 565 (7739): 305–311. doi:10.1038/s41586-018-0850-3.
- Romero-García, V., G. Theocharis, O. Richoux, A. Merkel, V. Tournat, and V. Pagneux. 2016. "Perfect and Broadband Acoustic Absorption by Critically Coupled Sub-Wavelength Resonators." *Scientific Reports* 6. doi:10.1038/srep19519.
- Salari-Sharif, Ladan, Lorenzo Valdevit, and Tobias A. Schaedler. 2014. "Energy Dissipation Mechanisms in Hollow Metallic Microlattices." *Journal of Materials Research* 29 (16): 1755–1770. doi:10.1557/jmr.2014.226.
- Schaedler, T. A., A. J. Jacobsen, A. Torrents, A. E. Sorensen, J. Lian, J. R. Greer, L. Valdevit, and W. B. Carter. 2011. "Ultralight Metallic Microlattices." *Science* 334 (6058): 962–965. doi:10.1126/science.1211649.
- Sha, Wei, Mi Xiao, Jinhao Zhang, Xuecheng Ren, Zhan Zhu, Yan Zhang, Guoqiang Xu, et al. 2021. "Robustly Printable Freeform Thermal Metamaterials." *Nature Communications* 12 (1): 7228. doi:10.1038/s41467-021-27543-7.
- Shao, Xiaofei, and Xiong Yan. 2022. "Sound Absorption Properties of Nanofiber Membrane-Based Multi-Layer Composites." *Applied Acoustics* 200 (November): 109029. doi:10.1016/j.apacoust.2022.109029.
- Shao, Chen, Yuanzhou Zhu, Houyou Long, Chen Liu, Ying Cheng, and Xiaojun Liu. 2022. "Metasurface Absorber for Ultra-Broadband Sound via Over-Damped Modes Coupling." *Applied Physics Letters* 120 (8): 083504. doi:10.1063/5.0080930.
- Song, Jian, Wenzhao Zhou, Yuejiao Wang, Rong Fan, Yinchu Wang, Junying Chen, Yang Lu, and Lixiao Li. 2019. "Octet-Truss Cellular Materials for Improved Mechanical Properties and Specific Energy Absorption." *Materials and Design* 173: 107773. doi:10.1016/j.matdes.2019.107773.
- Sun, Z. P., Y. B. Guo, and V. P. W. Shim. 2021. "Deformation and Energy Absorption Characteristics of Additively-Manufactured Polymeric Lattice Structures — Effects of Cell Topology and Material Anisotropy." *Thin-Walled Structures* 169: 108420. doi:10.1016/j.tws.2021.108420.
- Sun, Xiaojing, Fengchun Jiang, and Jiandong Wang. 2020. "Acoustic Properties of 316L Stainless Steel Lattice Structures Fabricated via Selective Laser Melting." *Metals* 10 (1): 111. doi:10.3390/met10010111.
- Surjadi, James Utama, Xiaobin Feng, Rong Fan, Weitong Lin, Xiaocui Li, and Yang Lu. 2021. "Hollow Medium-Entropy Alloy Nanolattices with Ultrahigh Energy Absorption and Resilience." *NPG Asia Materials* 13 (1), doi:10.1038/s41427-021-00306-y.
- Tang, Yufan, Shuwei Ren, Han Meng, Fengxian Xin, Lixi Huang, Tianning Chen, Chuanzeng Zhang, and Tian Jian Lu. 2017. "Hybrid Acoustic Metamaterial as Super Absorber for Broadband Low-Frequency Sound." *Scientific Reports* 7, doi:10.1038/srep43340.
- Tang, Yufan, Fengxian Xin, and Tian Jian Lu. 2019. "Sound Absorption of Micro-Perforated Sandwich Panel with Honeycomb-Corrugation Hybrid Core at High Temperatures." *Composite Structures* 226: 111285. doi:10.1016/j.compstruct.2019.111285.
- Wang, Zhonggang, Zichao Guo, Zhendong Li, and Kexin Zeng. 2021. "Coupling and Scaling Effect for Low-Frequency Broadband Sound Absorption via Vertex-Based Hierarchy." *Applied Physics Letters* 119 (17): 171903. doi:10.1063/5.0065278.
- Wang, Zhonggang, Zichao Guo, Zhendong Li, and Kexin Zeng. 2023. "Design, Manufacture, and Characterisation of Hierarchical Metamaterials for Simultaneous Ultra-Broadband Sound-Absorbing and Superior Mechanical Performance." *Virtual and Physical Prototyping* 18 (1), doi:10.1080/17452759.2022.2111585.
- Wang, Yixin, Hui Zhu, Wenyao Tu, Yuehong Su, Fatang Jiang, and Saffa Riffat. 2022. "Sound Absorption, Structure and Mechanical Behavior of Konjac Glucomannan-Based Aerogels with Addition of Gelatin and Wheat Straw." *Construction and Building Materials* 352 (October): 129052. doi:10.1016/j.conbuildmat.2022.129052.

- Woinnier, T., J. Reynes, A. Hafidi Alaoui, I. Beurroies, and J. Phalippou. 1998. "Different Kinds of Structure in Aerogels: Relationships with the Mechanical Properties." *Journal of Non-Crystalline Solids* 241 (1): 45–52. doi:10.1016/S0022-3093(98)00747-9.
- Yang, Wenjing, Jia An, Chee Kai Chua, and Kun Zhou. 2020. "Acoustic Absorptions of Multifunctional Polymeric Cellular Structures Based on Triply Periodic Minimal Surfaces Fabricated by Stereolithography." *Virtual and Physical Prototyping* 15 (2): 242–249. doi:10.1080/17452759.2020.1740747.
- Yang, Min, Shuyu Chen, Caixing Fu, and Ping Sheng. 2017. "Optimal Sound-Absorbing Structures." *Materials Horizons* 4 (4): 673–680. doi:10.1039/c7mh00129k.
- Yang, Xiaocui, Xinmin Shen, Panfeng Bai, Xiaohui He, Xiaonan Zhang, Zhizhong Li, Liang Chen, and Qin Yin. 2019. "Preparation and Characterization of Gradient Compressed Porous Metal for High-Efficiency and Thin-Thickness Acoustic Absorber." *Materials* 12 (9): 1413. doi:10.3390/ma12091413.
- Zeng, Kexin, Zhendong Li, Zichao Guo, Xifeng Liang, and Zhonggang Wang. 2022. "Acoustic Metamaterial for Highly Efficient Low-Frequency Impedance Modulation by Extensible Design." *Extreme Mechanics Letters* 56 (October): 101855. doi:10.1016/j.eml.2022.101855.
- Zhang, Zhong, Hongshuai Lei, Haiyang Yang, Mingji Chen, Changxian Wang, Heng Yang, and Daining Fang. 2021. "Novel Multifunctional Lattice Composite Structures with Superior Load-Bearing Capacities and Radar Absorption Characteristics." *Composites Science and Technology* 216: 109064. doi:10.1016/j.compscitech.2021.109064.
- Zhang, L., B. Song, J. J. Fu, S. S. Wei, L. Yang, C. Z. Yan, H. Li, L. Gao, and Y. S. Shi. 2020. "Topology-Optimized Lattice Structures with Simultaneously High Stiffness and Light Weight Fabricated by Selective Laser Melting: Design, Manufacturing and Characterization." *Journal of Manufacturing Processes* 56 (August): 1166–1177. doi:10.1016/j.jmapro.2020.06.005.
- Zhang, Lei, Bo Song, Jinliang Zhang, Yonggang Yao, Jian Lu, and Yusheng Shi. 2022. "Decoupling Microlattice Metamaterial Properties Through a Structural Design Strategy Inspired by the Hall–Petch Relation." *Acta Materialia* 238 (October): 118214. doi:10.1016/j.actamat.2022.118214.
- Zhang, Qiancheng, Xiaohu Yang, Peng Li, Guoyou Huang, Shangsheng Feng, Cheng Shen, Bin Han, et al. 2015. "Bioinspired Engineering of Honeycomb Structure - Using Nature to Inspire Human Innovation." *Progress in Materials Science* 74: 332–400. doi:10.1016/j.pmatsci.2015.05.001.
- Zhang, Zhi, Lei Zhang, Bo Song, Yonggang Yao, and Yusheng Shi. 2022. "Bamboo-Inspired, Simulation-Guided Design and 3D Printing of Light-Weight and High-Strength Mechanical Metamaterials." *Applied Materials Today* 26: 101268. doi:10.1016/j.apmt.2021.101268.
- Zheng, Xiaoyu, Howon Lee, Todd H. Weisgraber, Maxim Shusteff, Joshua DeOtte, Eric B. Duoss, Joshua D. Kuntz, et al. 2014. "Ultralight, Ultrastiff Mechanical Metamaterials." *Science* 344 (6190): 1373–1377. doi:10.1126/science.1252291.
- Zhou, Zhiling, Sibao Huang, Dongting Li, Jie Zhu, and Yong Li. 2021. "Broadband Impedance Modulation via Non-Local Acoustic Metamaterials." *National Science Review* 9 (8), doi:10.1093/nsr/nwab171.
- Zhou, Yong Feng, Chang Zhuang Yao, Qing Lin Yang, Lin Guo, and Lei Jiang. 2016. "Mechanical Properties of Diamond-Structured Polymer Microlattices Coated with the Silicon Nitride Film." *Advanced Engineering Materials* 18 (2): 236–240. doi:10.1002/adem.201500424.